N84-32168

FINAL REPORT

TITLE: Theoretical Design and Analysis of the Layered Synthetic Microstructure Optic for the Dual Path X-Ray Telescope

AUTHORS: D. L. Shealy, S. Chao

CONTRACT NO: NAS8-35916

PERIOD: MARCH 01 - MAY 31, 1984

DATE OF PUBLICATION: June 10, 1984

PRINCIPAL INVESTIGATOR: DAVID L. SHEALY, Ph.D
Physics Department, Room 202
Physical Sciences Building
University of Alabama in Birmingham
Birmingham, Alabama 35294
205-934-4736

PREPARED FOR: George C. Marshall Space Flight Center
Marshall Space Flight Center, Alabama 35812

DISTRIBUTION (17 copies + repro)
5/AS24D
1/AT01
10 + repro/ ES52, ATTN: R. B. Hoover
1/EM13A - 19
NASA Scientific and Technical Information Facility (1 copy + repro)

TABLE OF CONTENTS

ABSTRACT

A ray tracing analysis has been performed for several configurations for the inner channel of the dual path x-ray telescope, which is proposed to use the secondary mirror of the Stanford/MSFC Wolter-Schwarzschild telescope and a normal incident layered synthetic microstructure (LSM) mirror to form a secondary image near the front of the telescope. The LSM mirror shapes considered were spherical, ellipsoid, hyperboloid and constant optical path length (OPL) aspheric. Only for the constant OPL case gave good axial resolution. All cases had poor off axis resolution as judged by the RMS blur circle radius.

I. INTRODUCTION

During the past twenty years, the Wolter I Telescope[1] has been the most common telescope configuration used in x-ray astronomy. An interesting summary of work in the field thru 1978 is given in Ref. 2. The Wolter I telescope is a confocal paraboloid and hyperboloid operating at small glancing incidence angles as shown in Fig. 1. Normally, an aperture stop blocks light from directly hitting the secondary (hyperboloid), and the only mode for light to be imaged on the focal plane is through reflection from the paraboloid and then the hyperboloid, which will be termed the outer channel. A common problem with all glancing incidence x-ray telescopes is the small effective collecting area. A nested x-ray telescope[3] improves the telescope sensitivity, but fabrication costs and alignment problems arise.

As a result, Hoover[4] has proposed that the collecting area of a Wolter I x-ray telescope can be increased by constructing a third mirror such that the radiation incident upon the second surface (hyperboloid) of the type I telescope is reflected via a third mirror to the focal plane in concert with the radiation incident upon the outer mirror (paraboloid) of the type I x-ray telescope as shown in Fig. 2. Foreman and Cardone[5] have used the Wolter I x-ray telescope as a base system for the design of a three mirror x-ray telescope. The general result of Foreman's analysis is that the resolution of the outer channel is of the order of arc-seconds, while the resolution achieved via the inner channel is of the order of arc-minutes.

The present work is concerned with the development of a "dual path x-ray telescope" which permits x-rays that are directly incident upon the secondary mirror of the type I telescope (hyperboloid) to be reflected via a normal incident, layered synthetic microstructure (LSM) mirror located near the pseudo-focus of the hyperboloid to a second focal plane located near the structure of the type I telescope. See Fig. 3. This effort will design and analyze the LSM optic that will be utilized to couple the secondary of a Wolter/ Schwarzschild (WS) x-ray telescope to a 25 mm Ranicon x-ray detector with 50 micron pixel size. The specific tasks to be accomplished in this study are described in the "Scope of Work" given below.

SCOPE OF WORK

1. Generate equations for the internal secondary element of the Stanford/ MSFC X-ray Rocket Experiment Mirror by fitting the aspheric element to cubic spline function representations.

2. Develop ray trace equations for the inner channel of the Dual Path WS/LSM X-ray Telescope. This effort will include considerations of the LSM optic configured as a convex hyperboloid, ellipsoid, sphere or general aspheric element using constant optical path conditions.

3. Compute the RMS blur circle radius as a function of field angle on a flat image plane and evaluate the effects of defocusing the image plane.

4. Calculate the total range of angles over which the Wolter/LSM system will operate. Establishment of these angles includes considerations of the Ranicon position, LSM magnification and position and field of view of the Ranicon. Establish dimensions of the LSM to insure no vignetting of the primay beam, while providing maximum collection of the secondary beam.

5. In consultation with the MSFC Principal Investigator, select the final configuration of the mirror element that will be flown as part of the Rocket payload. Provide equations of the surface of the optic and the mirror parameters that will be required by the optical house for fabrication of the desired LSM element.

The specific principles, procedures and equations relating to the "Scope of Work" items 1 and 2 are given in section II of this report, and the results relating to items 3, 4, and 5 are given in Section III of this report.

II. MATHEMATICAL ANALYSIS

A. Ray Trace Equations for the Inner Channel of the Dual Path WS/LSM X-Ray Telescope

A general discussion of the ray tracing technique is given in Ref. 6. This report summarizes the equations used to ray trace the inner channel of the dual path WS/LSM x-ray telescope. The equations for the surface of the internal secondary mirror of the Stanford/MSFC WS x-ray telescope are given by

$$R_2 = d \sin\beta \qquad \text{(1a)}$$

$$Z_2 = d \cos\beta \qquad \text{(1b)}$$

with

$$1/d = \frac{\cos 4\alpha}{f}\left[\frac{1-\cos\beta}{1-\cos 4\alpha} + \frac{1}{2}(1+\cos\beta)\left(\frac{\tan^2(\beta/2)}{k} - 1\right)^{1+k}\right]$$

$$k = \tan^2(2\alpha)$$

$$\alpha = \beta^*/2 = 1/2 \arctan(r_0/f)$$

where f is the axial focal length of the WS telescope, which is equal to 50 in. for the inner Stanford/MSFC WS telescope, and r_o is the radius at the WS primary-secondary mirror intersection point, which is equal to 6.19 in. The surface parameter β varies from 7.057309 at the intersection point to 7.417018 at the rear of the telescope. (β^* specifies the intersection point of WS mirrors.) A discussion of the WS surface equations is given in Ref. 7. Table 1 presents a sample of the numerical data for the internal secondary mirror surface which was computed from Eq.(1a-b). Initially, it was proposed and was included in ITEM 1 of the SCOPE OF WORK to represent the WS secondary by a cubic spline polynomial to facilitate ray tracing. However, it has been found to be more efficient to generate a large table (N= 150) of R_2, Z_2 data from Eqs. (1a-b) and to use linear interpolation of the table to find the ray intercepts. The latter procedure is explained in the following discussion of ray tracing the inner channel of the WS/LSM Telescope.

Assume an incident ray with direction cosines

$$\underset{\sim}{A_o} = - \sin\alpha \; \hat{i} - \cos\alpha \; \hat{k} \tag{2}$$

strikes the entrance pupil at the point (X_o, Y_o, Z_o).

The entrance pupil is a plane normal to optical axis located at $Z_o = 60.5$ inches where the origin of the coordinate system is located at the focal point of the WS telescope. Polar coordinates are used to specify the points (X_o, Y_o) on the entrance pupil such that each ray passes thru an equal area.

From the transfer ray trace equations, the intercepts on the WS secondary mirror, which acts like the primary for the inner channel, are obtained by solving for β and φ_2:

$$R_2 \cos \varphi_2 = X_0 + (Z_2 - Z_0) \tan \alpha \tag{3a}$$

$$R_2 \sin \varphi_2 = Y_0 \tag{3b}$$

where R_2 and Z_2 are given by Eqs. (1a-b). The resulting nonlinear equations (3a-b) are difficult to solve in the present form. As an alternative approach, a linear interpolation technique has been developed. First, construct a table of data R_2 (I), Z_2 (I) for I=1,---, N from Eqs. (1a-b) for β within the interval [7.057309, 7.417018]. The interval containing a valid solution to

Eqs. (3a-b) must satisfy

$$F(I)\ F(I-1) \leq 0,$$

where

$$F(I) = R_2^2(I) - \{ [X_0 + (Z_2(I) - Z_0)\tan\alpha]^2 + Y_0^2 \} \tag{4a}$$

When the specific interval containing a solution to Eqs. (3a-b) is identified, then R_2, Z_2 are obtained by linear interpolation

$$R_2 = R_2(I-1) - F(I-1)\frac{[R_2(I) - R_2(I-1)]}{[F(I) - F(I-1)]} \tag{5a}$$

$$Z_2 = Z_2(I-1) - F(I-1)\frac{[Z_2(I) - Z_2(I-1)]}{[F(I) - F(I-1)]} \tag{5b}$$

where the fact that F(I) is equal to zero for the valid solutions R_2, Z_2.

The incident ray is reflected at the point R_2, Z_2 in the direction

$$\underset{\sim}{A}_1 = \underset{\sim}{A}_0 - 2\,\underset{\sim}{N}_1\,(\underset{\sim}{N}_1 \cdot \underset{\sim}{A}_0) \tag{6}$$

where $\underset{\sim}{N}_1$ is the unit normal to the surface

$$\underset{\sim}{N}_1 = \frac{-\cos\varphi_2\left(\frac{dZ_2}{dR_2}\right)\hat{i} - \sin\varphi_2\left(\frac{dZ_2}{dR_2}\right)\hat{j} + \hat{k}}{\left[1 + \left(\frac{dZ_2}{dR_2}\right)^2\right]^{1/2}} \tag{6a}$$

and

$$\frac{dZ_2}{dR_2} = \frac{(d'/d) - \tan\beta}{1 + (d'/d)\tan\beta} \tag{6b}$$

$$d' = [\ d\,(d)/d\beta\ ] \tag{6c}$$

The slope of the surface, (dZ_2/dR_2), at the point of reflection $(R_2,\ Z_2)$ is evaluated by linear interpolation.

The design condition for the LSM mirror is that an axial ray (α=0) incident upon the WS secondary mirror at the intersection point should be reflected by the LSM mirror to form an image along the optical axis at the

Ranicon detector location specified by Z_I. The axial intercept Z of the axial ray (α=0) reflected by the secondary WS mirror near the intersection point is give by

$$\bar{z} = z_2(\beta^*) - R_2(\beta^*) \frac{A_{1z}(\beta^*)}{A_{1x}(\beta^*)} \quad . \tag{7}$$

In the following sections 1 thru 4 equations are given for the design of the LSM mirror when this surface is a convex sphere, concaved ellipsoid, convex hyperboloid, or constant optical path aspheric. Also, specific ray trace equations for each LSM surface type are given.

1. Convex Sphere

The equation for the LSM spherical surface is given by

$$(Z_3 - Z_{03} + R_3)^2 + X_3^2 + y_3^2 = R_3^2 \tag{8}$$

where Z_{03} is the vertex of the surface and R_3 is the radius of curvature. See Fig. 4. Denoting the object and image distance by u and v, respectively, the magnification M of the LSM is given by

$$M = -\frac{v}{u} = \frac{z_I - z_{03}}{z_{03} - \bar{z}} \tag{9}$$

Adding and substracting $\bar{Z}$ to the numerator of Eq. (9) and solving for u, v, one obtains

$$u = \frac{z_I - \bar{z}}{M+1} \tag{9a}$$

$$-v = \frac{M}{M+1}\left(z_I - \bar{z} \right) \tag{9b}$$

Noting that $u = Z_{03} - \bar{Z}$, Eq (9a) yields

$$z_{03} = \frac{z_I + \bar{z} M}{1+M} \tag{10}$$

Solving the paraxial mirror equation,

$$\frac{1}{u} + \frac{1}{v} = -\frac{2}{R}$$

for R_3 gives

$$R_3 = \frac{2M\,(\bar{z} - z_I)}{M^2 - 1} \tag{11}$$

Numerical values for Z_{03} and R_3 with $Z_I = 60.5$ in. and several magnifications are given below

M	$-R_3$ (in)	z_{03} (in)
2	58.388	31.30
5	18.240	24.0
8	11.120	21.57

Transfer to the spherical surface is achieved by using standard ray tracing results[6]:

$$X_{3T} = X_2 + (Z_{03} - Z_2)\, A_{2x}/A_{2z} \tag{12a}$$

$$Y_{3T} = Y_2 + (Z_{03} - Z_2)\, A_{2y}/A_{2z} \tag{12b}$$

$$X_3 = X_{3T} + D\, A_{2x} \tag{12c}$$

$$Y_3 = Y_{3T} + D\, A_{2y} \tag{12d}$$

$$Z_3 = Z_{03} + D\, A_{2z} \tag{12e}$$

where

$$C D^2 - 2 D B + H = 0$$

$$B = A_{2z} - C\,(X_{3T} A_{2x} + Y_{3T} A_{2y})$$

$$H = C\,(X_{3T}^2 + Y_{3T}^2)$$

$$D = \{B - [B^2 - C H]^{1/2}\}$$

$$C = 1/R_3 \, .$$

The direction cosines of the reflected ray at the LSM mirror are given by

$$\underset{\sim}{A_3} = \underset{\sim}{A_2} - 2\,\underset{\sim}{N_3}\,(\underset{\sim}{A_2} \cdot \underset{\sim}{N_3}) \tag{13}$$

where

$$\underset{\sim}{N_3} = \frac{-\cos\varphi_3\left(\frac{dz_3}{dR_3}\right)\hat{i} - \sin\varphi_3\left(\frac{dz_3}{dR_3}\right)\hat{j} + \hat{k}}{\left[1 + \left(\frac{dz_3}{dR_3}\right)^2\right]^{1/2}}$$

The transfer equations to the image plane are given by

$$X_4 = X_3 + (z_4 - z_3)\,A_{3X}/A_{3z} \tag{14a}$$

$$Y_4 = Y_3 + (z_4 - z_3)\,A_{3Y}/A_{3z} \tag{14b}$$

The RMS blur circle radius on the image plane is computed from the ray intercepts (X_4, Y_4), using conventional techniques.[8]

2. Concave Ellipsoid

The equation for the LSM ellipsoid surface is given by

$$\frac{(z_3 - z_I - C_E)^2}{A_E^2} + \frac{R_3^{\,2}}{B_E^2} = 1 \tag{15}$$

where the ellipsoid constants are determined by requiring one foci to be at $\bar{Z}$ and the other foci to be at Z_I, along the optical axis. In terms of the magnification given by Eq. (9), one has

$$A_E = C_E \, (1+M) \big/ (M-1) \tag{15a}$$

$$B_E^2 = A_E^2 - C_E^2 \tag{15b}$$

$$C_E = \frac{1}{2} \left(z_I - \bar{z} \right) \tag{15c}$$

Numerical values for the ellipsoid coefficients for Z_I = 60.5 in. and several magnifications are given below

M	A_E (in)	B_E (in)	C_E (in)
2	65.68	61.92	21.89
5	32.84	24.48	21.89
8	28.15	17.69	21.89

The transfer ray trace equations yield the following results for intercepts with the LSM ellipsoid mirror.

$$C_2 X_3^2 + C_1 X_3 + C_0 = 0 \tag{16a}$$

$$Y_3 = Y_2 + (X_3 - X_2) A_{2Y} / A_{2X} \tag{16b}$$

$$Z_3 = Z_2 + (X_3 - X_2) A_{2Z} / A_{2X} \tag{16c}$$

where

$$C_0 = [X_2 A_{2Z} + (Z_I + C_E - Z_2) A_{2X}]^2$$
$$- (A_E/B_E)^2 [B_E^2 A_{2X}^2 - (X_2 A_{2Y} - Y_2 A_{2X})^2]$$

$$C_1 = -2X_2 A_{2Z}^2 - 2 A_{2X} A_{2Z} (Z_I + C_E - Z_2)$$
$$+ (A_E/B_E)^2 (-2X_2 A_{2Y}^2 + 2 Y_2 A_{2X} A_{2Y})$$

$$C_2 = A_{2Z}^2 + (A_E/B_E)^2 (A_{2X}^2 + A_{2Y}^2) .$$

Equations (13-14a,b) are applied for reflection and transfer to the image plane.

3. Convex Hyperboloid

The equation for the LSM hyperboloid surface is given by

$$\frac{(z_3 - z_I - C_H)^2}{A_H^2} - \frac{R_3^2}{B_H^2} = 1 \qquad (17)$$

where the hyperboloid constants are determined by requiring one foci to be at $\bar{Z}$ and the other foci to be at Z_I, along the optical axis. In terms of the magnification given by Eq. (9), one has

$$A_H = C_H (M-1) / (M+1) \qquad (17a)$$

$$B_H^2 = C_H^2 - A_H^2 \qquad (17b)$$

$$C_H = (z_I - \bar{z})/2 \, . \qquad (17c)$$

Numerical values for the hyperboloid coefficients for Z_I = 60.5 in. and for several magnifications are given below

M	A_H (in)	B_H (in)	C_H (in)
2	7.2985	20.643	21.895
5	14.5970	16.32	21.895
8	17.02	13.762	21.895

The transfer ray trace equations yield the following results for the intercepts with the LSM hyperboloid mirror

$$D_2 X_3^2 + D_1 X_3 + D_0 = 0 \tag{18a}$$

$$Y_3 = Y_2 + (X_3 - X_2) A_{2Y}/A_{2X} \tag{18b}$$

$$Z_3 = Z_I + C_H - A_H \left[1 + \frac{(X_3^2 + Y_3^2)}{B_H^2} \right]^{1/2} \tag{18c}$$

where

$$D_0 = [X_2 A_{2Z} - (Z_2 - Z_I - C_H) A_{2X}]^2$$
$$- (A_H/B_H)^2 [B_H^2 A_{2X}^2 + (X_2 A_{2Y} - Y_2 A_{2X})^2]$$

$$D_1 = 2 X_2 A_{2Z}^2 + 2 A_{2X} A_{2Z} (Z_2 - Z_I - C_H)$$
$$+ (A_H/B_H)^2 (-2 A_{2X} A_{2Y} Y_2 + 2 X_2 A_{2Y}^2)$$

$$D_2 = A_{2Z}^2 - (A_H/B_H)^2 (A_{2X}^2 + A_{2Y}^2) .$$

Equations (13-14a,b) are applied for reflection and transfer to the image plane.

4. <u>General Aspheric with Constant Optical Path Length</u>

The equation for the constant optical path length (OPL) LSM aspheric surface is obtained by requiring for axial rays (α=0) the OPL to be constant for all rays passing thru the entrance pupil (Z_o = 60.5 in) and imaging at the focal point (0, Z_I). From Fig. 4 for an arbitrary ray in the entrance pupil, the OPL is given by

$$OPL = z_0 - z_2 + [(z_3 - z_2)^2 + (R_3 - R_2)^2]^{1/2} \tag{19}$$

$$+ [(z_3 - z_I)^2 + R_3^2]^{1/2} .$$

The LSM surface coodinates X_3, Z_3 are also constrained to satisfy the transfer ray tracing equation

$$R_3 = (z_3 - \bar{z}) A_{2R} / A_{2z} \tag{20}$$

where A_{2R} is the R component of $\underset{\sim}{A}_2$. Eliminating R_3 between Eqs.(19-20) gives

$$A_3 z_3^2 + B_3 z_3 + C_3 = 0 \tag{21}$$

where $A_3 = 1 + \bar{b}^2 - b^2$

$$B_3 = 2 z_I - 2 \bar{b}^2 \bar{z}^2 - 2 b c$$

$$C_3 = z_I^2 + \bar{b}^2 \bar{z}^2 - c^2$$

$$a = OPL - z_0 + z_2$$

$$b = (2z_I + 2z_2 + 2\sigma R_2)/(2a)$$

$$c = (a^2 + z_I^2 - z_2^2 - 2\sigma z R_2 - R_2^2)/(2a)$$

The valid solution to Eq. (21) is given by

$$z_3 = \frac{-B_3 - (B_3^2 - 4A_3C_3)^{1/2}}{2A_3} \tag{22}$$

Equations (20) and (22) are parametric surface equations for the constant OPL LSM aspheric surface. A cubic spline polynomial representation for the aspheric surface is presented in Section B.

For off axis rays ($\alpha \neq 0$), the intercepts on the aspheric LSM surface are obtained by solving the transfer ray trace equations

$$X_3 = X_2 + (z_3 - z_2)A_{2x}/A_{2z} \tag{23a}$$

$$Y_3 = Y_2 + (z_3 - z_2)A_{2y}/A_{2z} \tag{23b}$$

where (X_3, Y_3, Z_3) must satisfy Eqs (20), (22). Equations (20), (22), and (23a-b) have been solved by a linear interpolation technique. First, construct a table of data R_3 (I), Z_3 (I) for I = 1, ---, N from Eqs. (20), (22) for the full aperture. Then the interval containing a valid solution to Eqs. (23a-b) must satisfy

$$G(I)\ G(I-1) \leq 0 \tag{24}$$

where

$$G(I) = R_3^2(I) - \left\{ \left[X_2 + (Z_3(I) - Z_2)\left(A_{2x}/A_{2z}\right)\right]^2 + \left[Y_2 + (Z_3(I) - Z_2)\left(A_{2y}/A_{2z}\right)\right]^2 \right\}$$

When the specific interval containing a solution to Eqs. (23a-b) is identified, then Z_3 is obtained by linear interpolation

$$Z_3 = Z_3(I-1) - G(I-1)\,\frac{[Z_3(I) - Z_3(I-1)]}{[G(I) - G(I-1)]} \tag{25}$$

Now X_3 and Y_3 are computed from Eqs. (23a-b). Equations (13-14a-b) are applied for reflection and transfer to the image plane where the slope (dZ_3/dR_3) of the constant OPL aspheric is computed the condition

$$\frac{d\,OPL}{d\,R_3} = 0 \tag{26}$$

which can be rewritten using Eq. (19).

$$\frac{dZ_3}{dR_3} = \frac{(R_2 - R_3)\,S - R_3 T}{(Z_3 - Z_2)\,S + (Z_3 - Z_1)\,T} \tag{27}$$

where

$$S = \left[(z_3 - z_2)^2 + (R_3 - R_2)^2 \right]^{-1/2}$$

$$T = \left[(z_3 - z_I)^2 + R_3^2 \right]^{-1/2}$$

B. Cubic Spline Representation for the LSM Constant Optical Path Length Mirror of the Stanford/MSFC Dual Path X-ray Telescope

To facilitate fabrication of the constant OPL LSM aspheric mirror, a cubic spline polynomial function has been fit to the numerical data generated from Eqs. (20) and (22), using a least squared fitting subroutine ICSFKU[9]. In order to fit a set of N data points (Z_I, R_I) with a cubic spline polynomial, one first divides the domain of independent variables, Z_I, into NK-1 subintervals. The end points for each subinterval is given by an array ZK(I), I = 1,2, NK. Then, the cubic spline polynomial between the end points ZK(I) and ZK(I-1) is given by

$$R_3(z_{3i}) = C(I,3)\left[z_{3i} - ZK(I)\right]^2 + C(I,2)\left[z_{3i} - ZK(I)\right]^2$$

$$+ C(I,1)\left[z_{3i} - ZK(I)\right] + Y(I) \qquad (28)$$

where the coefficients C(I,J), ZK (K), and Y (I) with J = 1, 2, 3, I = 1, 2, ---, NK-1, and K = 1, 2, ---, NK. are determined by the subroutine ICSFKU[9] and Z_{3i} belongs to the Ith subinterval. For one hundred fifty (N=150) data points and twenty subintervals (NK= 21), the leasted error obtained in fitting the data with the cubic spline polynomial is of the order of 10^{-13}. Tables 2, 3 and 4 present the cubic spline coefficients for LSM aspheric surface for magnifications M = 2, 5, 8, respectively.

III. RESULTS

In Chapter II, all equations for ray tracing the inner channel of the Dual Path X-ray Telescope were presented for cases when the LSM mirror was a convex sphere, concave ellipsoid, convex hyperboloid or a constant OPL aspheric. Section 1 will present the RMS spot radius analysis of the inner channel for M = 2, 5, 8x, the spread in the angle of incidence over the LSM optic and a vignetting analysis of the primary beam by the LSM optic. Section 2 will present a recommended final configuration of the LSM optic.

1. RMS Blur Circle Radius Analysis and Geometrical Properties of LSM Optic

Before presenting the RMS blur circle radius results for the inner channel of the Dual Path X-ray Telescope, it is useful to discuss the imaging properties of the WS secondary mirror when illuminated directly by axial rays. For axially incident light, the WS secondary mirror is a poorly imaging element with a focal length of 34 inches. (The focal length is defined as the distance along a ray from the WS intersection point to the optical axis.) For three regions of the WS secondary mirror (WS intersection point, average WS secondary radius and minimum radius), rays have been traced to compute the axial intercept $\bar{Z}$ and the location of the meridional caustic points (X_{2c}, Z_{2c}).[10-11] This data is given in Table 5. From the rotational symmetry of the WS secondary mirror, rays from a ring an equal distance from the optical axis will be imaged at $\bar{Z}$. Such an image is known as the saggital caustic.[10-11] The length of the saggital caustic is equal to the spherical aberration of the system. Thus, the WS secondary has a large spherical aberration of 3.66 inches. As a result of this imaging defect, the meridional caustic (X_{2c}, Z_{2c}), which is the loci of image points contained within the meridional plane (x-z), is spread out over very large distances. It is interesting to note that both the meridional and saggital caustic surfaces for a paraboloid degenerate to a point at the focus. Thus, the design assumption used for the inner chanel of the dual path x-ray telescope is not satisfied for the spherical, ellipsoid, or hyperboloid LSM mirror, and poor RMS blur circule results should be expected in these cases.

Figures 5, 6, and 7 present the RMS blur circle radius as a function of field angles for the inner channel of the dual path X-ray telescope over the image plane locatd at the front stop of the WS telescope Z_I = 60.5 in.), when the convex sphere, concaved ellipsoid, and convex hyperboloid surfaces are used for the LSM mirror. In all cases, the RMS blur circle radii are too large for these systems to be used for imaging purposes. This behavior results from the large spherical aberration of the WS secondary mirror. In order to overcome the imaging defect of the inner channel of the dual path x-ray telescope an aspheric surface must be used for the LSM mirror. Initially, one may consider the LSM aspheric mirror could be designed by

(1) Abbe Sine Condition, which for collimated rays from infinity requires for all rays in the entrance pupil

$$h/\sin\theta = \text{constant}$$

where h is the height of ray in this entrance pupil and θ is the angle ray makes with the optical axis at the image plane.

(2) Constant optical path length condition for all rays in the entrance pupil.

Referring to Fig. 4, one notes that rays with small h in the entrance pupil are incident upon the image plane with larger θ. Thus, the Abbe Sine Condition will inherently be violated by the inner channel of the dual path x-ray telescope. However, the constant OPL condition can be used to design on LSM aspheric optical element with zero spherical aberration. For the latter aspheric LSM the on axis resolution will be good but off axis resolution will deteriorate quickly due to coma and other aberrations.

Figures 8 and 9 present the RMS blur circle radius for the constant OPL aspheric LSM mirror over an image plane located at the front (Z_I = 60.5 in) and the back (Z_I = 41.3 in) of the WS telescope. One notes that the RMS over the image plane located closer to the LSM element is approximately 10% smaller than for the image plane located at the front of the WS telescope. Also, the RMS blur circle radius is equal to zero for $\alpha = 0$ as a result of the constant OPL design condition. However, the RMS rapidly increases for off axis rays, since the inner channel of the dual path x-ray telescope does not obey the Abbe Sine Condition. After consultation with MSFC Principal Investigator, all further analysis of the inner channel of the dual path x-ray telescope has been restricted to considering the constant OPL LSM mirror with the image plane located at the front (Z_I = 60.5 in) of the WS telescope. Figure 10 presents an expanded view of Fig. 8 for field angles from 0 to 20 arc minutes.

In order to evaluate the imaging properties of the inner channel of the dual path x-ray telescope and the Ranicon detector (50 micron = 2 mil (.002 in) pixel and 25 mm = 1 inch square area), it is useful to know the effective focal length of the system:

M	f_{Total} (in)
2	68
5	170
8	272

The angular half widths of the detector in the entrance pupil for M = 2, 5, 8 are given by

M	$0.5\,in / f_{Total}$ (arc-min)
2	26
5	10
8	6

These results give a first order optics approximation for the field of view of the dual path x-ray telescope system. Since the angles of incidence of rays on the WS secondary are very large, paraxial optics is not very accurate for predicting optical behavior of the dual path x-ray optical system. Figure 11 presents the average x coordinate of the blur circle on the image plane as a function of field of view. By comparing Figs. 10 and 11, it is clear that in none of the cases considered will the off axis resolution be very good, since the RMS blur circle radii are larger than the average image position. The higher magnification case spreads out the average image position more. However, it is known for glancing incident system that the RMS over estimates actual resolution by a factor of 2 to 3.[12] But, for the present hybrid telescope, it is not clear what is the relationship between RMS blur circle radii and measured resolution. In order to more accurately predict measured resolution for the dual path x-ray telescope, the FWHM of line spread function should be evaluated. From Figs. 10 and 11, one may estimate the M=8x system to have a maximum field of view of 10 to 15 arc-min with a resolution of a few arc minutes.

Besides the resolution of the inner channel of the dual path x-ray telescope, there are several geometrical properties of the LSM optic which are of interest. The following data gives the maximum and minimum angles of incidence, measured with respect to the LSM normal for field of view angles from 0 to 20 arc minutes

M	ϕ_{min} (rad)	ϕ_{MAX} (rad)
2	0.13524	0.15582
5	0.10735	0.1253
8	0.10034	0.11767

This information will be useful in fabrication of the LSM mirror in controlling the layer spacings. Another important geometrical property of the LSM optic is the possible vignetting of the primary WS beam by the LSM. The following data describes the minimum radius of the primary beam R_{PB}, at the location of the LSM for a full field of view of 20 arc minutes and the maximum radius of LSM optic, R_{3max}.

M	R_{PB} (in)	R_{3MAX} (in)
2	3.7612	3.4614
5	2.812	2.0704
8	2.4958	1.6071

Since in all cases R_{3max} is less than R_{PB}, there is no vignetting of the primary beam by the LSM optic in the present configuration.

2. Recommended Final Configuration of LSM Optic

Based on the results presented in Figs. 5-9, it is clear that only the constant OPL LSM configuration will form a useful system. From Fig. 11 it follows that the larger magnification, i.e., M=8, spreads out the image on the detector more than smaller M. However, to determine a realistic increase of resolution, the FWHM of the line spread function should be evaluated before fabricating the constant OPL LSM mirror. Table 4 presents the cubic-spline representation for the M=8 case.

IV. CONCLUSIONS

Although the collecting area of the Stanford/MSFC WS Telescope is increased by approximately 29 sq. in., the off axis RMS blur circle radii for the constant OPL LSM mirror are very large. Before proceeding with the fabrication of a constant OPL LSM element for the dual Path x-ray telescope, the FWHM of the line spread function should be analyzed for the inner channel to determine if the system will perform at an acceptable level of resolution. Otherwise, an LSM element could be placed near the primary focus of the WS Telescope to magnify the primary image.

REFERENCES

1. H. Wolter, Ann. Phys. 10 94(1952).

2. J.H. Underwood, Am. Scientist 66.4, 476 (1978).

3. J.M. Davis, A.S. Krieger, J.K. Silk, R.C. Chase, Proc. SPIE 184, 96 (1979).

4. R. B. Hoover, Three Mirror Clancing Incidence System for X-Ray Telescope, US Patent Office, No. 3821556 (1974).

5. J.W. Foreman, and J.M. Cardone, Design and Mathematical Analysis of a Three Mirror X-Ray Telescope Based on ATM-S056 X-Ray Telescope Hardware, Final Report under contract NA 58-2730, Marshall Space Flight Center, Huntsville, Ala. (1973).

6. Optical Design: Military Standardization Handbook, #MIL-HDBK-141, US Government Printing Office, Washington, DC (1962).

7. R.C. Chase, L.P. Van Speybroech, Applied Optics 12.5, 1042 (1973).

8. R. J. Gagnon, JOSA 58 (1968).

9. International Mathematics and Statistical Libraries, Edition 6, Houston, Texas (1979).

10. David L. Shealy, Applied Optics 15.10, 2588 (1976).

11. Donald G. Burkhard, David L. Shealy, APPLIED OPTICS, 20.5 897 (1981).

12. David L. Shealy, "Analysis of NOAA-MSFC GOES X-ray Telescope," Final Report submitted to George C. Marshall Space Flight Center, Order No H-34373 B, August 24, 1979.

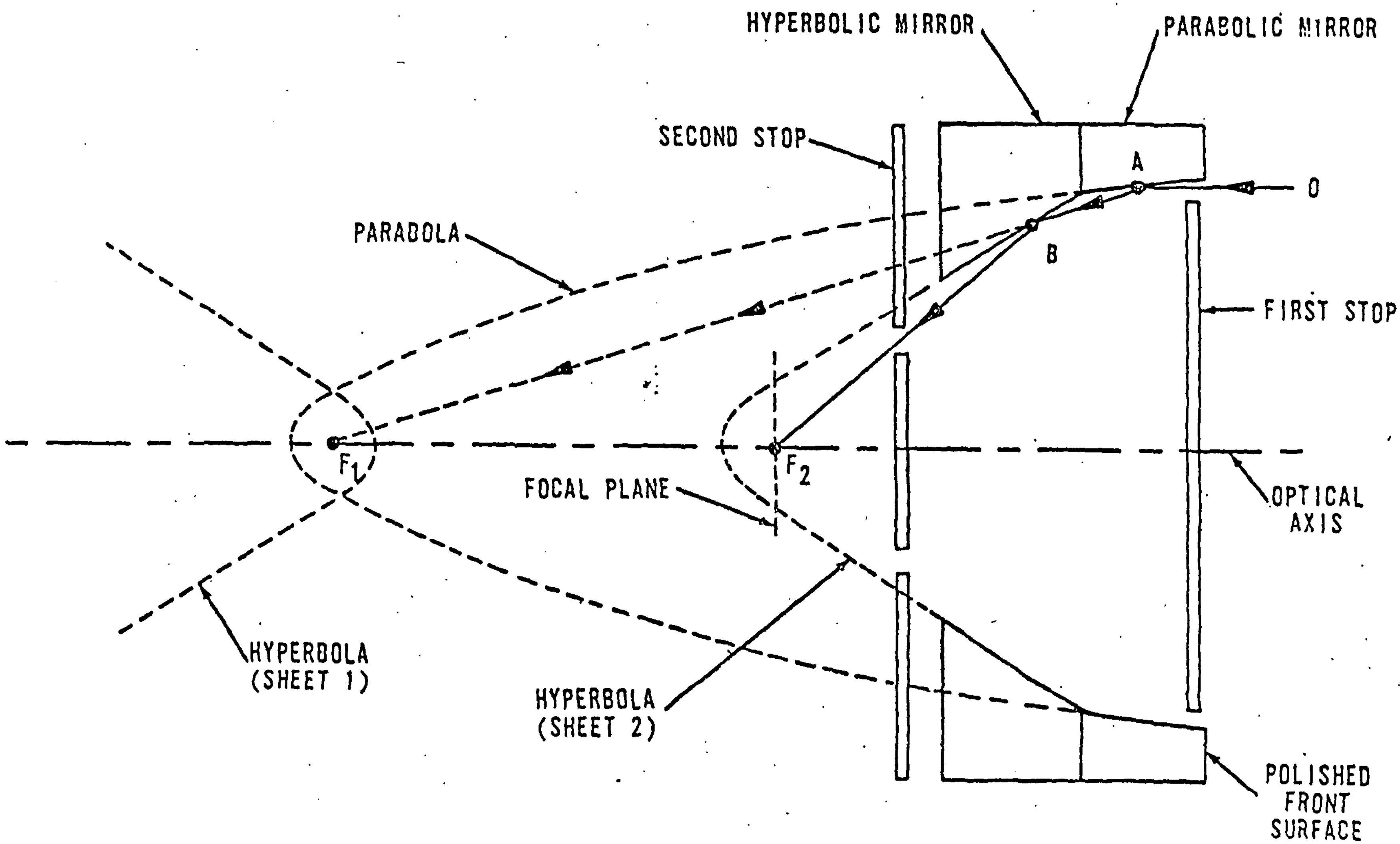

Fig. 1. Wolter I X-Ray Telescope Configuration.

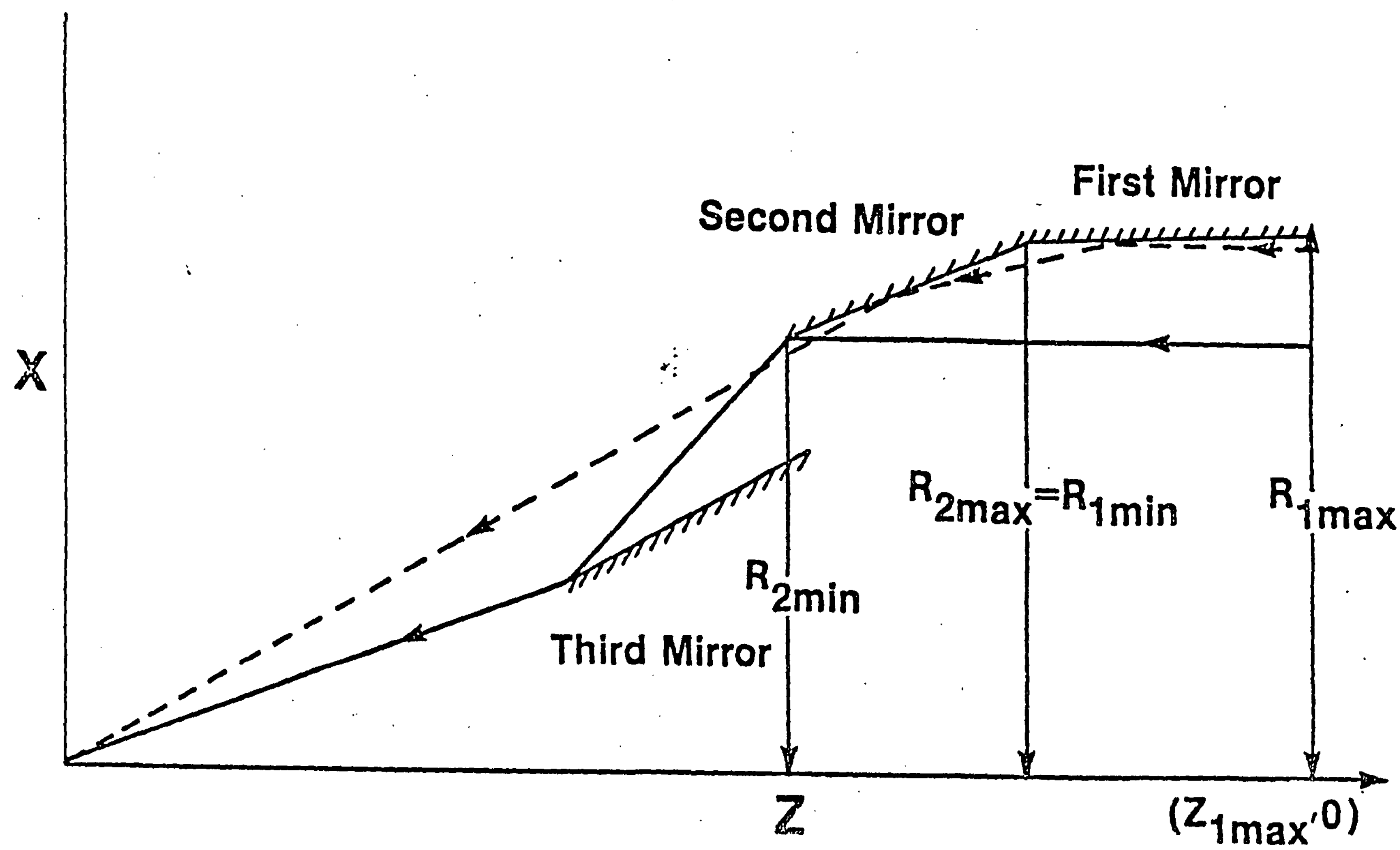

Fig. 2. Cross sectional diagram of a three mirror x-ray telescope.

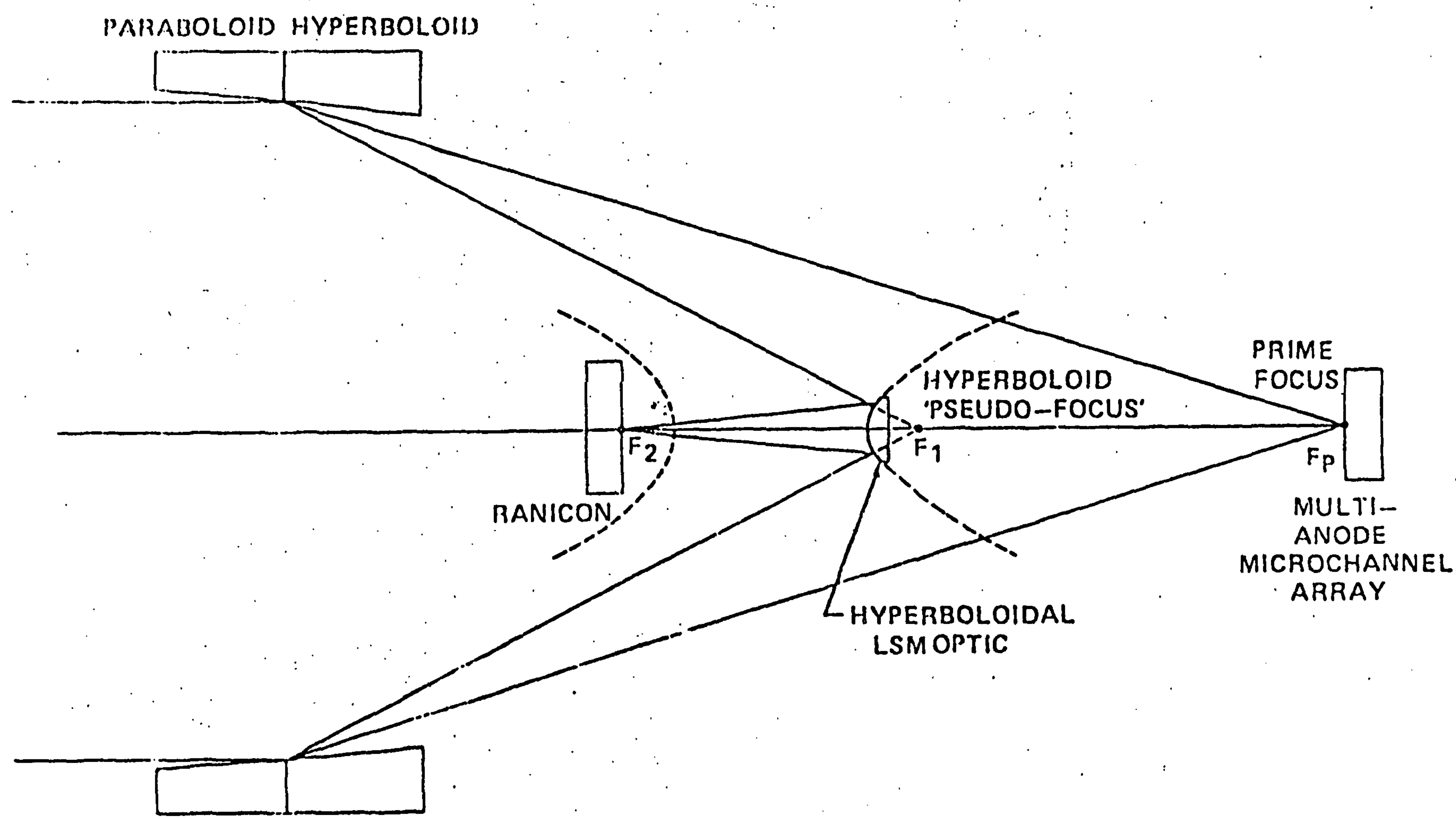

Fig. 3. Dual Path X-Ray Telescope.

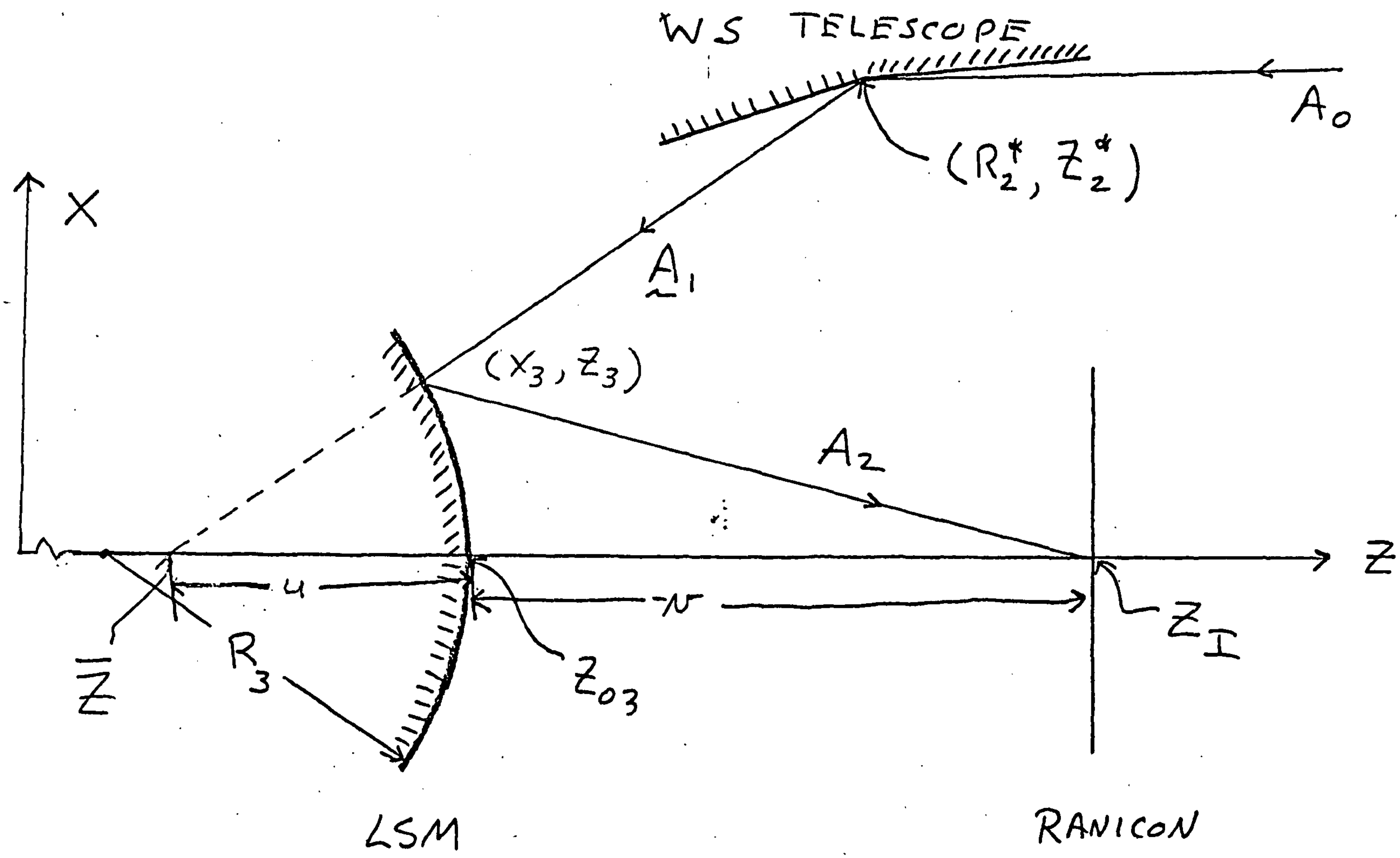

Fig. 4. Dual Path X-ray Telescope with Convex Spherical Reflector.

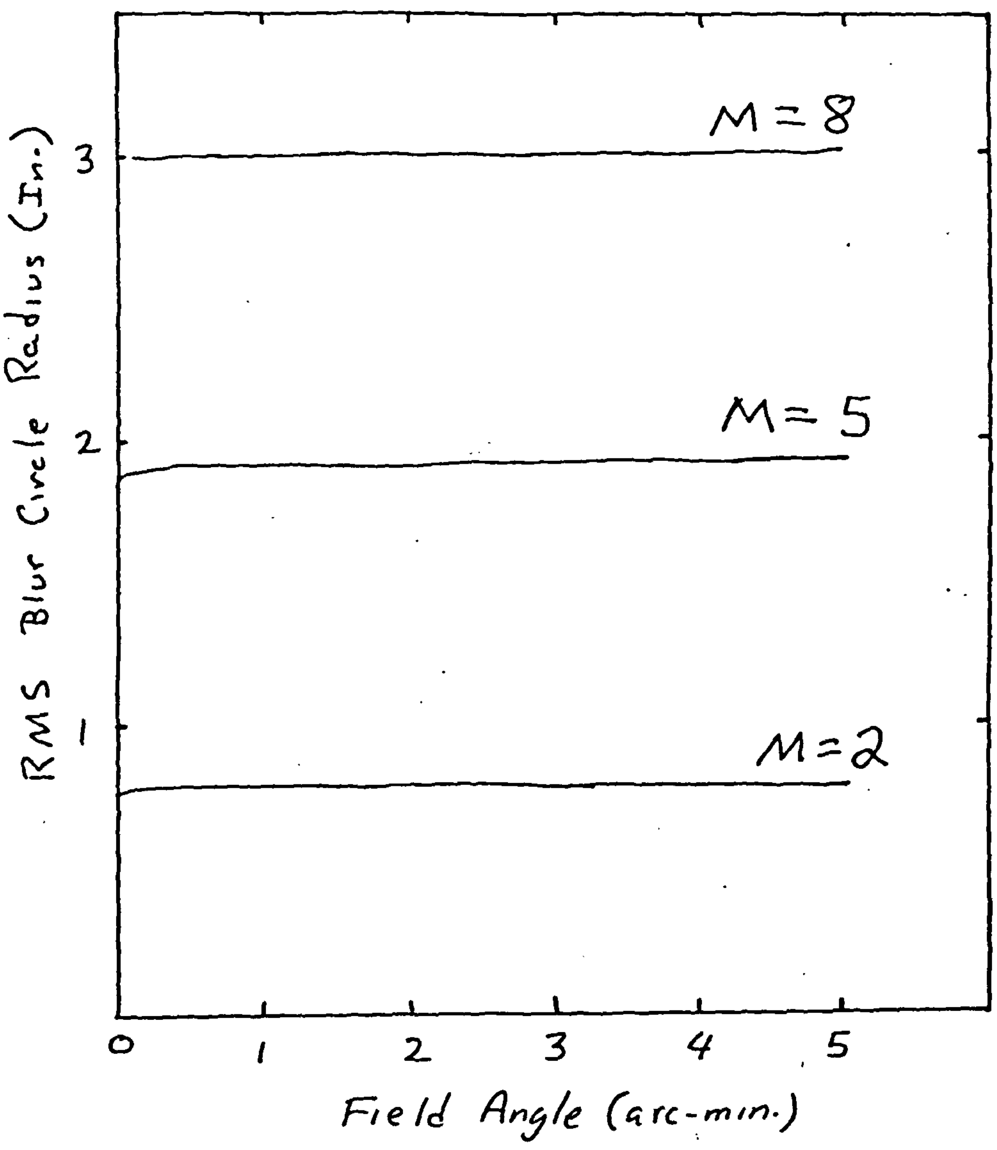

Figure 5

RMS Blur Circle Radius versus Field Angle for Spherical LSM Mirror.

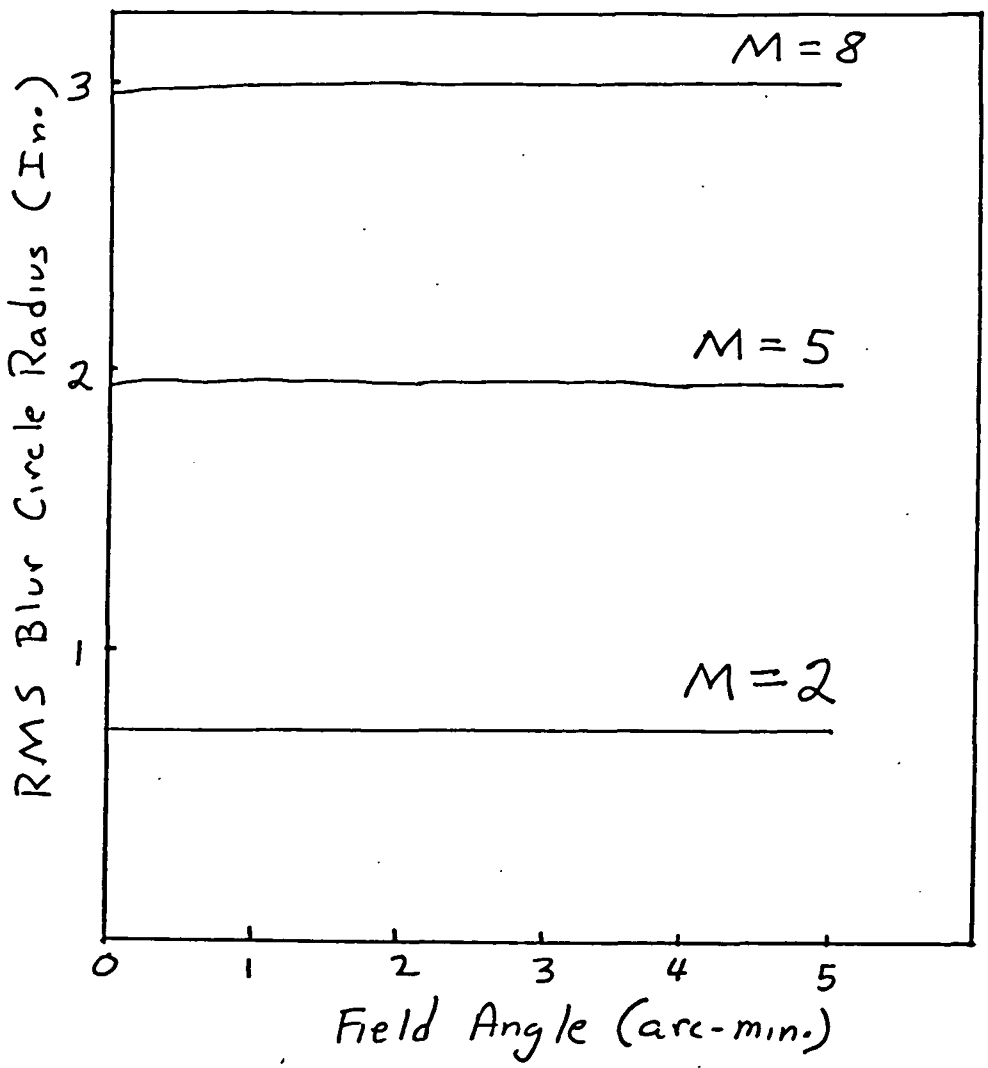

Figure 6

RMS Blur Circle Radius versus Field for Ellipsoid LSM Mirror.

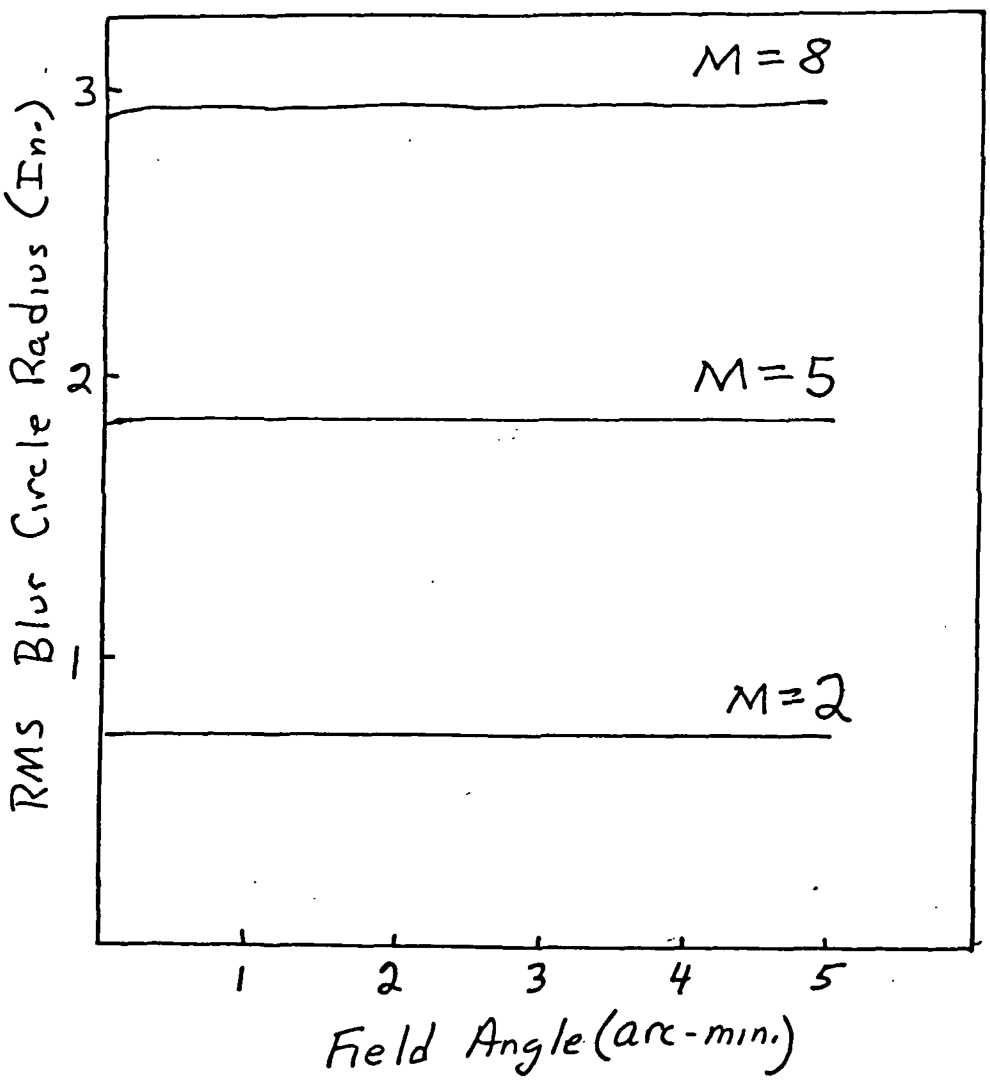

Figure 7

RMS Blur Circle Radius versus Field Angle for Hyperboloid LSM Mirror.

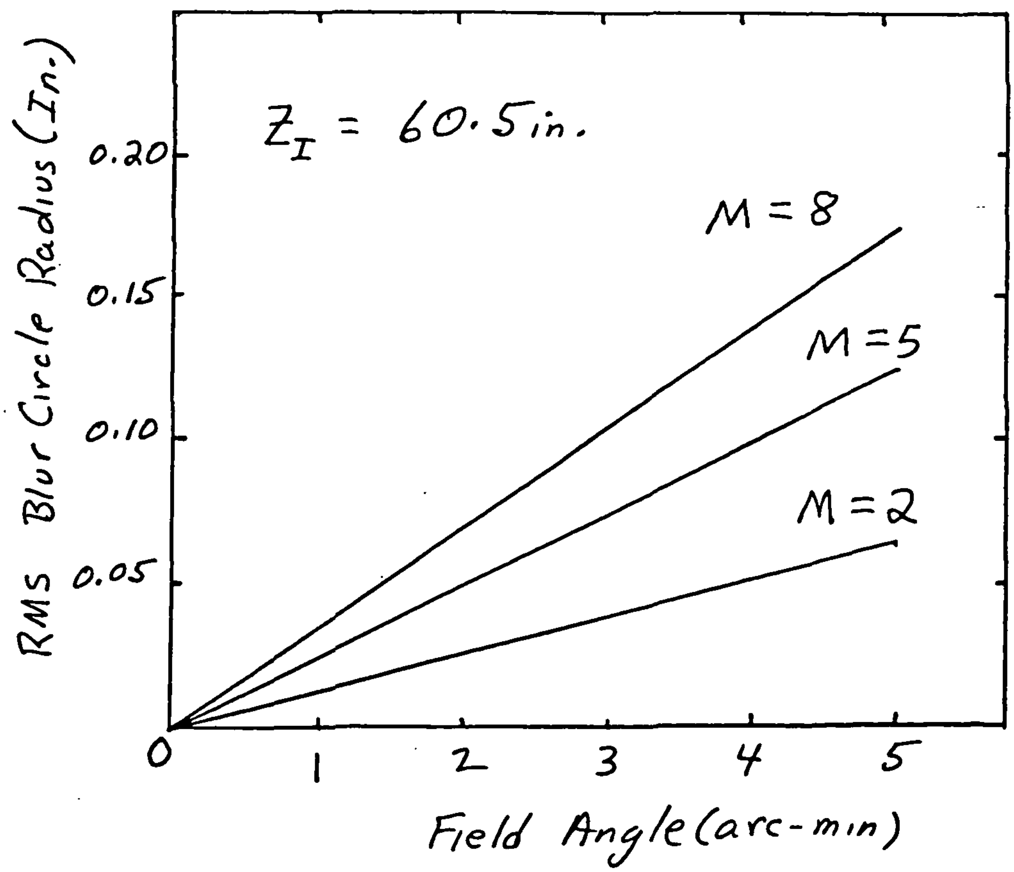

Figure 8

RMS Blur Circle Radius versus Field Angle for Constant Optical Path Length Aspherical LSM Mirror.

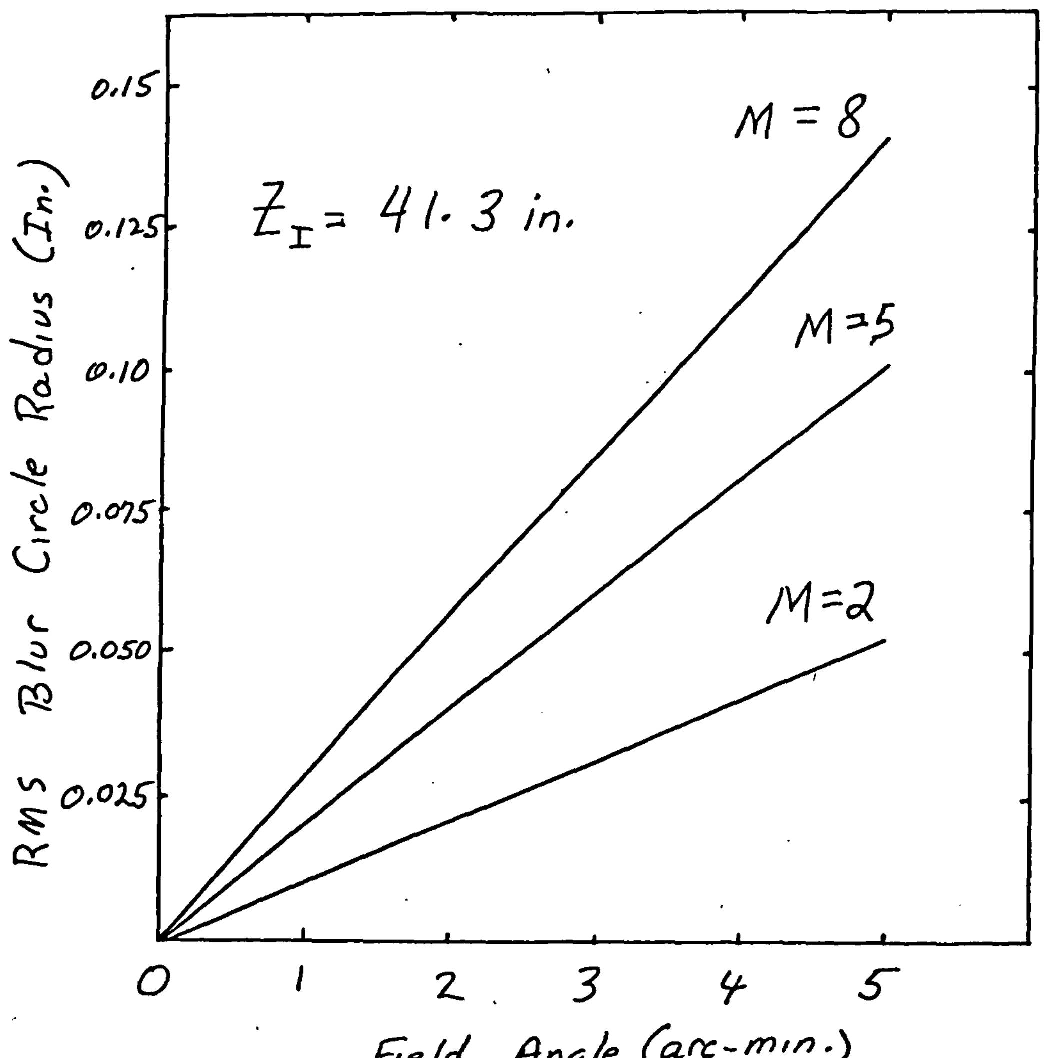

Figure 9

RMS Blur Circle Radius versus Field Angle for Constant Optical Path Length Aspherical LSM Mirror.

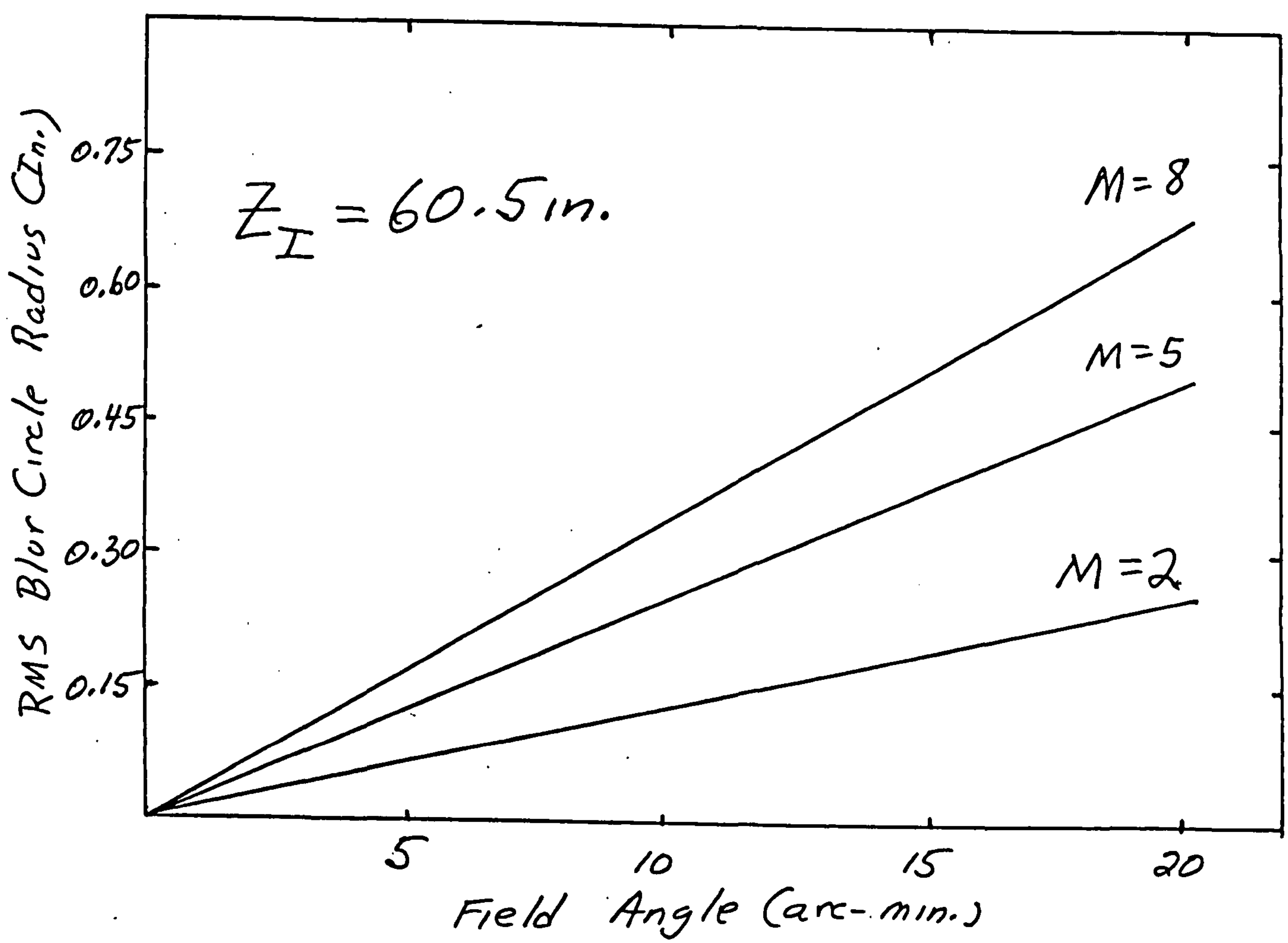

Figure 10

RMS Blur Circle Radius versus Field Angle for Constant Optical Path Length Aspherical LSM Mirror.

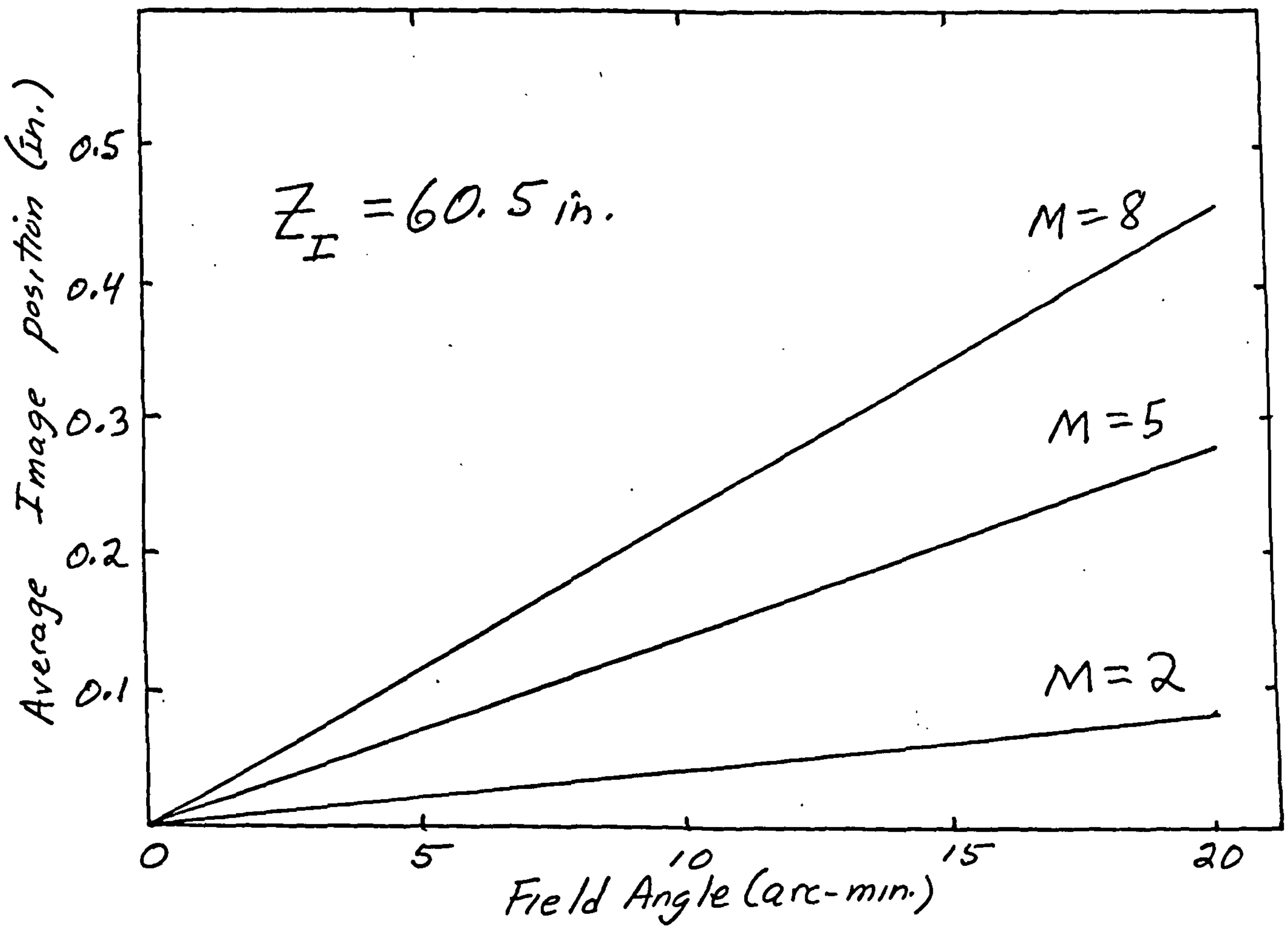

Figure 11

Average Image Position versus Field Angle for Constant Optical Path Length Aspherical LSM Mirror.

Table 1

NUMERICAL DATA
FOR THE INTERNAL SECONDARY MIRROR SURFACE
OF THE STANFORD/MSFC TELESCOPE

β	R_2 (in)	Z_2 (in)
7.057309	6.190	50.0
7.090010	6.106241	49.09362
7.126344	6.015758	48.1170
7.162678	5.928081	47.17269
7.199013	5.843122	46.25948
7.235347	5.760772	45.37606
7.271681	5.680920	44.52110
7.308015	5.603459	43.69334
7.344350	5.528286	42.89158
7.380684	5.455301	42.11465
7.417018	5.384410	41.36147

TABLE 2

CUBIC SPLINE COEFFICIENTS FOR LSM ASPHERIC WITH M = 2x.

K	$R_3(K)$	$Z_3(K)$
1	0.346137D 01	0.312755D 02
2	0.342844D 01	0.312766D 02
3	0.339033D 01	0.312780D 02
4	0.335255D 01	0.312794D 02
5	0.331509D 01	0.312807D 02
6	0.327793D 01	0.312821D 02
7	0.324109D 01	0.312835D 02
8	0.320454D 01	0.312849D 02
9	0.316828D 01	0.312863D 02
10	0.313230D 01	0.312878D 02
11	0.309661D 01	0.312892D 02
12	0.306119D 01	0.312906D 02
13	0.302605D 01	0.312921D 02
14	0.299118D 01	0.312935D 02
15	0.295658D 01	0.312950D 02
16	0.292227D 01	0.312964D 02
17	0.288822D 01	0.312979D 02
18	0.285452D 01	0.312994D 02
19	0.282110D 01	0.313008D 02
20	0.278813D 01	0.313023D 02
21	0.271475D 01	0.313056D 02

I	Y(I)	C(I,1)	C(I,2)	C(I,3)
1	0.346137D 01	-0.285795D 02	0.164859D 03	-0.170237D 04
2	0.342844D 01	-0.282039D 02	0.158935D 03	-0.159612D 04
3	0.339033D 01	-0.277801D 02	0.152416D 03	-0.149331D 04
4	0.335255D 01	-0.273708D 02	0.146278D 03	-0.140049D 04
5	0.331509D 01	-0.269754D 02	0.140485D 03	-0.131456D 04
6	0.327793D 01	-0.265933D 02	0.135015D 03	-0.123573D 04
7	0.324109D 01	-0.262237D 02	0.129842D 03	-0.116305D 04
8	0.320454D 01	-0.258661D 02	0.124945D 03	-0.109669D 04
9	0.316828D 01	-0.255200D 02	0.120302D 03	-0.103382D 04
10	0.313230D 01	-0.251848D 02	0.115901D 03	-0.981378D 03
11	0.309661D 01	-0.248601D 02	0.111701D 03	-0.920304D 03
12	0.306119D 01	-0.245455D 02	0.107742D 03	-0.894700D 03
13	0.302605D 01	-0.242406D 02	0.103875D 03	-0.808125D 03
14	0.299118D 01	-0.239450D 02	0.100367D 03	-0.859206D 03
15	0.295658D 01	-0.236587D 02	0.966197D 02	-0.664681D 03
16	0.292227D 01	-0.233810D 02	0.937108D 02	-0.931621D 03
17	0.288822D 01	-0.231125D 02	0.896170D 02	-0.435693D 03
18	0.285452D 01	-0.228525D 02	0.877002D 02	-0.123313D 04
19	0.282110D 01	-0.226026D 02	0.822605D 02	-0.136200D 03
20	0.278813D 01	-0.223621D 02	0.816611D 02	-0.202130D 04

TABLE 3

CUBIC SPLINE COEFFICIENTS For LSM ASPHERIC WITH M = 5x.

K	$R_3(K)$	$Z_3(K)$
1	0. 207037D 01	0. 239577D 02
2	0. 203894D 01	0. 239597D 02
3	0. 200256D 01	0. 239621D 02
4	0. 196645D 01	0. 239645D 02
5	0. 193063D 01	0. 239670D 02
6	0. 189508D 01	0. 239693D 02
7	0. 185980D 01	0. 239717D 02
8	0. 182478D 01	0. 239741D 02
9	0. 179003D 01	0. 239765D 02
10	0. 175552D 01	0. 239789D 02
11	0. 172128D 01	0. 239813D 02
12	0. 168728D 01	0. 239836D 02
13	0. 165354D 01	0. 239860D 02
14	0. 162005D 01	0. 239884D 02
15	0. 158681D 01	0. 239907D 02
16	0. 155386D 01	0. 239931D 02
17	0. 152115D 01	0. 239954D 02
18	0. 148881D 01	0. 239977D 02
19	0. 145675D 01	0. 240001D 02
20	0. 142520D 01	0. 240024D 02
21	0. 135742D 01	0. 240073D 02

I	Y(I)	C(I,1)	C(I,2)	C(I,3)
1	0. 207037D 01	−0. 152166D 02	0. 190461D 02	−0. 341442D 02
2	0. 203894D 01	−0. 151382D 02	0. 188341D 02	−0. 339481D 02
3	0. 200256D 01	−0. 150479D 02	0. 185885D 02	−0. 337631D 02
4	0. 196645D 01	−0. 149591D 02	0. 183448D 02	−0. 335558D 02
5	0. 193063D 01	−0. 148715D 02	0. 181030D 02	−0. 333691D 02
6	0. 189508D 01	−0. 147853D 02	0. 178630D 02	−0. 331672D 02
7	0. 185980D 01	−0. 147004D 02	0. 176249D 02	−0. 329957D 02
8	0. 182478D 01	−0. 146167D 02	0. 173884D 02	−0. 328924D 02
9	0. 179003D 01	−0. 145344D 02	0. 171531D 02	−0. 326365D 02
10	0. 175552D 01	−0. 144533D 02	0. 169201D 02	−0. 330589D 02
11	0. 172128D 01	−0. 143734D 02	0. 166844D 02	−0. 319770D 02
12	0. 168728D 01	−0. 142948D 02	0. 164569D 02	−0. 348318D 02
13	0. 165354D 01	−0. 142175D 02	0. 162096D 02	−0. 295517D 02
14	0. 162005D 01	−0. 141414D 02	0. 160002D 02	−0. 418496D 02
15	0. 158681D 01	−0. 140667D 02	0. 157043D 02	−0. 211867D 02
16	0. 155386D 01	−0. 139933D 02	0. 155550D 02	−0. 629752D 02
17	0. 152115D 01	−0. 139214D 02	0. 151122D 02	0. 574528D 00
18	0. 148881D 01	−0. 138510D 02	0. 151163D 02	−0. 118143D 03
19	0. 145675D 01	−0. 137828D 02	0. 142939D 02	0. 347495D 02
20	0. 142520D 01	−0. 137166D 02	0. 145331D 02	−0. 267428D 03

TABLE 4

CUBIC SPLINE COEFFICIENTS FOR LSM ASPHERIC WITH M = 8x.

K	$R_3(K)$	$Z_3(K)$
1	0. 160705D 01	0. 215202D 02
2	0. 157611D 01	0. 215225D 02
3	0. 154028D 01	0. 215252D 02
4	0. 150471D 01	0. 215278D 02
5	0. 146942D 01	0. 215304D 02
6	0. 143438D 01	0. 215331D 02
7	0. 139960D 01	0. 215357D 02
8	0. 136508D 01	0. 215383D 02
9	0. 133080D 01	0. 215409D 02
10	0. 129677D 01	0. 215435D 02
11	0. 126299D 01	0. 215461D 02
12	0. 122945D 01	0. 215487D 02
13	0. 119615D 01	0. 215513D 02
14	0. 116311D 01	0. 215538D 02
15	0. 113031D 01	0. 215564D 02
16	0. 109779D 01	0. 215590D 02
17	0. 106551D 01	0. 215615D 02
18	0. 103360D 01	0. 215640D 02
19	0. 100198D 01	0. 215666D 02
20	0. 970884D 00	0. 215690D 02
21	0. 904935D 00	0. 215743D 02

I	Y(I)	C(I,1)	C(I,2)	C(I,3)
1	0. 160705D 01	−0. 136145D 02	0. 125576D 02	−0. 142932D 02
2	0. 157611D 01	−0. 135576D 02	0. 124600D 02	−0. 144416D 02
3	0. 154028D 01	−0. 134918D 02	0. 123452D 02	−0. 146088D 02
4	0. 150471D 01	−0. 134269D 02	0. 122294D 02	−0. 147463D 02
5	0. 146942D 01	−0. 133628D 02	0. 121128D 02	−0. 148971D 02
6	0. 143438D 01	−0. 132994D 02	0. 119954D 02	−0. 150270D 02
7	0. 139960D 01	−0. 132368D 02	0. 118772D 02	−0. 151771D 02
8	0. 136508D 01	−0. 131750D 02	0. 117581D 02	−0. 153598D 02
9	0. 133080D 01	−0. 131140D 02	0. 116380D 02	−0. 154466D 02
10	0. 129677D 01	−0. 130538D 02	0. 115175D 02	−0. 159732D 02
11	0. 126299D 01	−0. 129944D 02	0. 113932D 02	−0. 154974D 02
12	0. 122945D 01	−0. 129357D 02	0. 112729D 02	−0. 176746D 02
13	0. 119615D 01	−0. 128779D 02	0. 111361D 02	−0. 143317D 02
14	0. 116311D 01	−0. 128209D 02	0. 110255D 02	−0. 229937D 02
15	0. 113031D 01	−0. 127649D 02	0. 108487D 02	−0. 909822D 01
16	0. 109779D 01	−0. 127096D 02	0. 107790D 02	−0. 380883D 02
17	0. 106551D 01	−0. 126555D 02	0. 104881D 02	0. 519344D 01
18	0. 103360D 01	−0. 126024D 02	0. 105275D 02	−0. 769125D 02
19	0. 100198D 01	−0. 125509D 02	0. 994732D 01	0. 276990D 02
20	0. 970884D 00	−0. 125010D 02	0. 101536D 02	−0. 185975D 03

Table 5

WS SECONDARY MIRROR IMAGING DATA
All units are inches

R_2	Z_2	$\overline{Z}$	X_{2c}	Z_{2c}
6.188	49.984	16.709	-2.53	3.10
5.755	45.318	14.750	-35.53	-103.9
5.386	41.385	13.049	-31.01	-150.03